Journal of Radiation Research and Applied Sciences 19 (2026) 102489

Contents lists available at ScienceDirect

Journal of Radiation Research and Applied Sciences

journal homepage: www.journals.elsevier.com/journal-of-radiation-research-and-applied-sciences

Delineation of subsurface structure and radiological hazards utilizing integrated airborne magnetic and spectrometric data

Waheed H. Mohamed [a], Tamader Alhazani [b], Mohamed Elsadek M. Sabra [c], Basma A. El-Badry [b], Mabrouk Sami [d], Ioan V. Sanislav [e,*], El Saeed R. Lasheen [a,**]

[a] Geology Department, Faculty of Science, Al-Azhar University, P.O. Box 11884, Cairo, Egypt
[b] Physics Department, Faculty of Science, Imam Mohammad Ibn Saud Islamic University (IMSIU), Riyadh, Saudi Arabia
[c] Egyptian Mineral Resources Authority, Po. Box 11517, Abbassiya, Cairo, Egypt
[d] Geosciences Department College of Science United Arab Emirates University, Al Ain, United Arab Emirates
[e] Economic Geology Research Centre (EGRU), College of Science and Engineering, James Cook University, Townsville, QLD, 4811, Australia

ARTICLE INFO

Keywords:
Gamma-ray spectrometry
Environmental monitoring
Magnetic method
Structural controls

ABSTRACT

The research integrates gamma-ray spectrometric surveys, radiometric mapping, and magnetic data interpretation to evaluate uranium anomalies, thorium and potassium distributions, radiogenic heat production, and their correlation with lithological units and structural trends in the Kulet Niheidat-Abu Had, Central Eastern Desert of Egypt. Results reveal that the uranium concentrations are anomalously high in the Duwi, Tarawan, and Dakhla formations, as well as in younger granitic intrusions, with values reaching up to 20.34 ppm. The thorium enrichment is particularly associated with granitic and metavolcanic rocks, while potassium concentrations are elevated in granites and fanglomerates. Radiogenic heat production exceeds 0.71 $\mu W/m^3$ in crystalline lithologies, highlighting their contribution to crustal thermal regimes. Magnetic analysis delineates three major shear zones (S1-S3) trending Northwest–Southeast and Northeast–Southwest, which exert significant control on fluid migration and mineralization processes. Radiation exposure and dose rates, ranging between 0.15 and 0.69 mSv/y, remain below international safety thresholds, indicating no significant health risks to the local population. Collectively, the findings demonstrate a strong spatial correlation between radioelement anomalies, lithological variations, and tectonic structures, underscoring the mineral potential of the study area and its relevance for both environmental monitoring and resource exploration.

1. Introduction

Natural radioactivity has long been employed in mineral exploration due to the diagnostic properties of certain radioisotopes. These isotopes, characterized by unstable nuclei, undergo radioactive decay processes that transform them into isotopes of other elements while emitting particles and releasing energy (Abdel-Aal et al., 2024; Akpanowo et al., 2020). The concentrations of these elements, their radiation emissions, and their geochemical associations offer useful information about the geological environment and the localization of economically significant mineralization. A notable example is apatite mineralization, which can be detected through gamma radiation surveys because of its frequent association with radioactive elements such as Th and U (Abbady et al., 2005; Baturin & Kochenov, 2001; Lasheen et al., 2022). Gamma radiation, produced during nuclear de-excitation processes, possesses significantly higher energy than visible light. When integrated with other geophysical and geological datasets, gamma-ray measurements enhance surface information and serve as a powerful tool in geological investigations (Bücker & Rybach, 1996, 1996, 1996; Eisenbud & Gesell, 1997; Guo et al., 2020; Youssef & Elkhodary, 2013). The natural physicochemical processes occurring within the Earth's crust, including rock weathering and soil formation, strongly influence the distribution of K, Th, and particularly U (El-Qassas et al., 2023). Consequently, surface and near-surface features derived from geological mapping can be effectively correlated with radiometric survey data, improving the interpretation of lithological variations and mineralization patterns. Magnetic surveying represents another widely applied geophysical technique. It is primarily used to delineate ore bodies at depth, map

---

* Corresponding author.
** Corresponding author.
E-mail addresses: ioan.sanislav@jcu.edu.au (I.V. Sanislav), elsaeedlasheen@azhar.edu.eg (E.S.R. Lasheen).

https://doi.org/10.1016/j.jrras.2026.102489
Received 5 April 2026; Received in revised form 19 May 2026; Accepted 1 June 2026
Available online 3 June 2026

subsurface geological structures such as faults (Lasheen, El-Badry, Mohamed, et al., 2025; Lasheen, Elyaseer, et al., 2024; Saada, 2016), and support environmental assessments (Lasheen, El-Badry, Kamh, et al., 2025; Lasheen et al., 2026).

Together, radiometric and magnetic methods provide complementary datasets that enhance the resolution of subsurface geological models. Gamma-ray spectrometric surveys, in particular, have become indispensable in environmental studies, geological mapping, and mineral exploration (IAEA, 2010). These surveys enable the identification of anomalous zones enriched in uranium and other radioactive elements, while also supporting environmental monitoring programs. The objective of this study is to investigate the natural radioactivity of rocks within the Central Eastern Desert of Egypt, assess their environmental implications, and identify anomalous U zones. Furthermore, the study aims to evaluate potential correlations between structural trends and U anomalies, thereby contributing to a more comprehensive understanding of the geologic framework and mineralization processes in the region.

2. Geological setting

The Central Desert of Egypt, the northernmost part of the Arabian-Nubian Shield (ANS (Abdelaal et al., 2025; Lasheen et al., 2023; Lasheen, Sami, et al., 2024; Saleh et al., 2025); is geologically diverse. It features Precambrian rocks alongside a sedimentary succession dating from the Upper Cretaceous to the Quaternary. The study area is located in the Central Eastern Desert of Egypt, bounded by latitudes 26°16′00″–26°38′00″ N and longitudes 32°38′00″–33°12′00″ E (Fig. 1a). The Precambrian rocks include metavolcanics (acidic to intermediate) exposed in the north eastern side this area (Fig. 1b). They are intruded by younger granites (medium relief, pink color, and sheared along shear zones). From the other side, the area under examination is dominated by the Abu Had syncline. This 40 km long, NW-SE trending fold, shaped by Gulf of Suez tectonics, is intersected by major NW-SE and NE-SW fault systems (El-Sawy et al., 2011). The area's sedimentary succession comprises a series of distinct formations: the Taref, Quseir, Duwi, Dakhla, Tarawan, Esna, and Thebes. The oldest exposed unit, the Taref Formation, overlies the Quseir Formation and is predominantly fine-to medium-grained, well-sorted sandstone with occasional shale interbeds. The underlying Early Campanian Quseir Formation consists of variegated shales formed under marginal-to shallow-marine conditions. The overlying Campanian-early Maastrichtian Duwi Formation is divided into three phosphorite members. The lower member consists of weathered phosphate bands with shale, chert, and claystone. In contrast, the middle member is markedly thicker, containing gray to black shale, siltstone, marl, and thin phosphate layers with shale that darkens upwards and contains iron bands. The upper member includes phosphate, shale, and dolomitic lenses, culminating in a fossiliferous limestone cap. In the study area, the Dakhla Formation is exposed at Gabal Abu Had's northwestern side, situated between the underlying Duwi Formation and the overlying Tarawan Formation. This approximately 83 m thick siliciclastic mudstone sequence spans the Maastrichtian to Danian interval and is divided into two members: the lower Hamama Marl Member (~28 m of pale-gray marl and calcareous shale) and the upper Beida Shale Member (~55 m of greenish-gray laminated shale, claystone, and marl).

Overlying the Dakhla is the Tarawan Formation, a stratigraphically key unit composed of snow-white, massive chalk. At Gabal Abu Had, this Middle Paleocene formation has distinctive lithology clearly separates the Dakhla and Esna formations. On the north-western side of the study area, the Esna Formation stratigraphically succeeds the Tarawan Formation and is itself overlain by the Thebes Formation. Comprising about 40 m of calcareous shale and marl (collectively known as the “Esna Shale”), it is divided into three distinct members: the basal El-Hanadi Member (gray marl and calcareous shale), the middle El-Shaghab Member (greenish-gray claystone, shale, and marl with a phosphatic shale bed), and the upper Abu Had Member (dark marl that grades upward into limestone. Conformably overlying the Esna Formation, the Thebes Formation forms the north-western escarpment of Gabal Abu Had. This unit, exceeding 20 m in thickness, represents a widespread Lower Eocene (Ypresian) shallow-shelf chalk facies.

The study area's Quaternary deposits are unconsolidated Wadi-fill sediments, conglomerate, sand, and gravel: categorized as old alluvium, old Wadi deposits, and recent Wadi sediments.

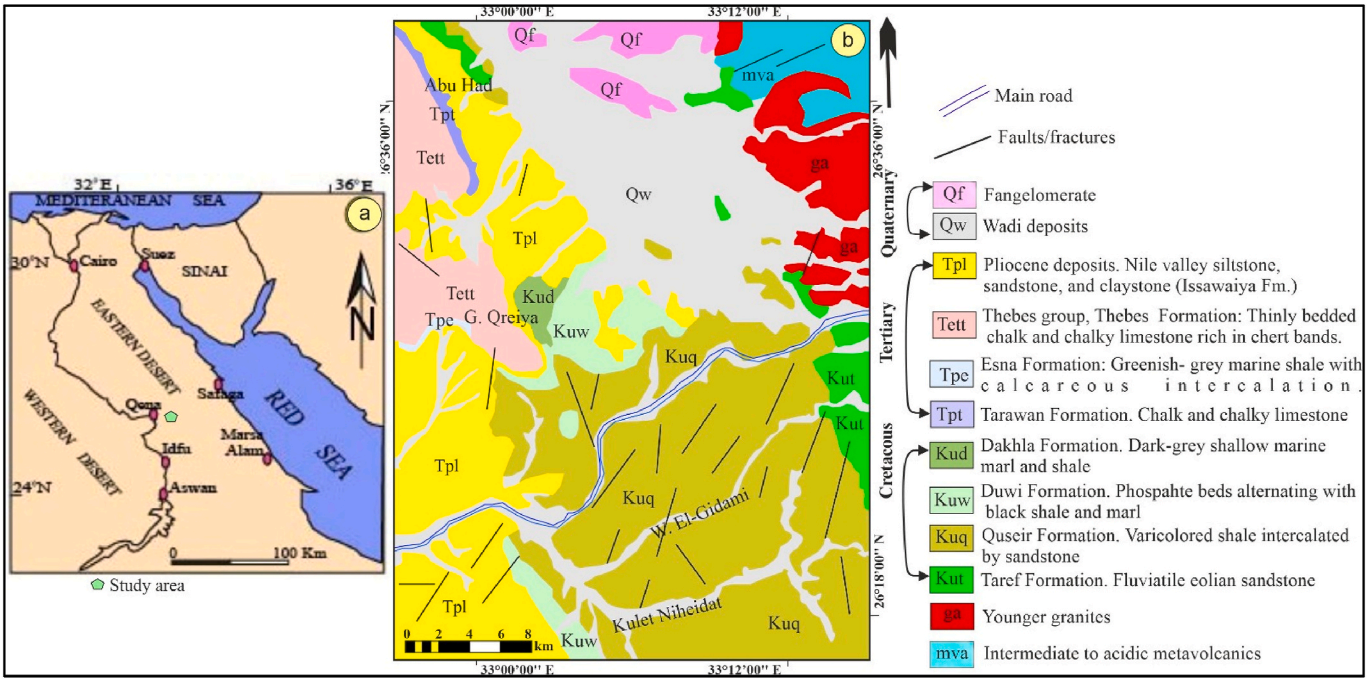

Fig. 1. a) location map; **b**) geological map of the study area (EGSMA, 1981).

3. Methodology

The spectrometric and magnetic measurements analyzed in this study were acquired in 1982 during the MPGAP project, a collaborative effort between the Egyptian General Petroleum Corporation (EGPC), the Egyptian Geological Survey and Mining Authority (EGSMA), and the Aero-Service Division of Western Geophysical Company of America. The survey was conducted as an airborne magnetic and gamma-ray spectrometric campaign covering a large portion of the Eastern Desert and a smaller area of the Central Western Desert of Egypt. Its primary objective was to provide geophysical data to support the identification and evaluation of mineral, petroleum, and groundwater resources. Traverse lines were flown in a N45°E orientation with an approximate spacing of 1 km, while tie lines were oriented N135°E and spaced at about 10 km intervals. The survey was carried out at a flight altitude of 120 m above ground level. A high-sensitivity 256-channel gamma-ray spectrometer system with an energy resolution of 12 keV/channel was used for the airborne spectrometric survey. The system consisted of two groups of detectors: (1) primary downward-looking detectors composed of three detector packages, each containing four thallium-activated sodium iodide crystals [NaI(Tl)] used for measuring terrestrial gamma radiation, with a total detector volume of 3072 cubic inches (50.34 L); and (2) secondary upward-looking detectors composed of two NaI(Tl) crystals with a total volume of 512 cubic inches (8.39 L), used for measuring atmospheric radon contributions (Aero-Service, 1984).

The recorded aero-spectrometric data then passed through several corrections (scattering effects, background effects, atmospheric effects, altitude correction … etc.) and produced as contoured sheets. The airborne spectrometric data were subsequently processed and interpreted using the OASIS Montaj software package (Geosoft Program (Geosoft Program, 2014).

3.1. *Gamma ray spectrometric data*

In the present study, the qualitative and quantitative evaluation of gamma-ray spectrometric data is examined using statistical analysis. The acquired spectrometric datasets including total count (TC), equivalent uranium (eU), equivalent thorium (eTh), and potassium concentration (K%) were processed as digital grid maps. From these primary variables, three elemental ratios (eU/eTh, eU/K, and eTh/K) were calculated to enhance lithological and geochemical discrimination.

3.2. *Statistical analysis*

Basic statistical parameters, including the mean, minimum, maximum, standard deviation, and tests of normality, were computed for each variable (Table 1). The statistical evaluation of the airborne gamma-ray spectrometric data primarily relies on the coefficient of variability (CV%) (Hervé, 2010; Nairy & Aruna Rao, 2003), which is calculated as:

$$\mathrm{CV}\ (\%) = (\sigma\ /\ \mathrm{X}) \times 100 \tag{1}$$

where σ represents the standard deviation and X denotes the arithmetic mean. A CV value less than 100% indicates a tendency toward normal distribution of the data. The CV analysis was applied to all seven variables for each lithological unit. Lower CV values indicate greater homogeneity within a rock unit, whereas higher values reflect increased heterogeneity. The results show that all rock units exhibit CV values below 100%, indicating that the spectrometric variables for these units generally follow a normal distribution and display a high degree of internal homogeneity.

3.3. *Ternary radioelement maps*

Ternary radioelement maps are a visual tool that combines the spatial distribution of key gamma-emitting elements, K, Th, and U, into a single color-coded image. By assigning each element to a primary color channel, variations in element ratios become immediately apparent, allowing geologists to detect subtle lithological differences and boundaries. The eU channel is mapped in blue because its signal often contains more noise than the K and eTh channels, and the human eye is less sensitive to blue variations. Applying a threshold to the total count ensures that low-activity, noisy regions do not distort the visual interpretation, enhancing the contrast and clarity of meaningful data (IAEA, 2010).

Ternary maps are particularly valuable because many rock types have characteristic K/eTh/eU ratios. By visualizing these ratios, geologists can identify homogeneous lithological units, detect transitions between rock types, and support regional geological mapping, mineral exploration, and environmental radiometric assessments (Lasheen, El-Badry, Mohamed, et al., 2025; Lasheen et al., 2026).

3.4. *Radiogenic heat production (RHP)*

During radioactive decay, a portion of the atomic mass is converted into energy. With the exception of a very small fraction carried away by neutrinos and antineutrinos during β^- and β^+ decay or electron capture, nearly all of this energy is transformed into heat. Each radioactive decay series produces characteristic gamma-ray energy peaks, while the continuous background observed in gamma-ray spectra results from Compton scattering and photoelectric absorption processes (AlZahrani et al., 2011).

The total gamma-ray emission, which reflects the combined radioactive decay of uranium, thorium, and potassium, can be used to estimate radiogenic heat production (RHP). An empirical relationship proposed by (Bücker & Rybach, 1996) relates bulk radiogenic heat production to the total gamma-ray count (TC) measured by borehole logging tools as:

$$\mathrm{RHP}\ \left(\mu\mathrm{W}\ /\ \mathrm{m}^3\right) = 0.0158 \times [\mathrm{TC}\ (\mathrm{API}) - 0.8] \tag{2}$$

The API (American Petroleum Institute) unit is a standardized measure of natural gamma radiation. According to Ellis (1987), the API value is calculated using the following equation:

$$\mathrm{API} = 16 \times \mathrm{K}\ (\%) + 8 \times \mathrm{U}\ (\mathrm{ppm}) + 4 \times \mathrm{Th}\ (\mathrm{ppm}) \tag{3}$$

The RHP reflects the contribution of radioactive elements, primarily U, Th, and K, to the internal heat budget of the Earth's crust. The spatial distribution observed in the study area indicates significant lithological

Table (1)
Statistics of the airborne gamma-ray spectrometric data for all rock units of the study area.

Variables	TC(μR/h)	eTh (ppm)	eU (ppm)	K (%)	eU/eTh	eU/K	eTh/K
Minimum	5.0	0.7	5.0	0.1	0.1	0.1	1.8
Maximum	86.8	12.6	86.8	3.6	5.9	50.8	19.3
X	28.6	5.0	28.6	1.0	0.7	5.2	6.0
σ	11.1	1.9	11.1	0.6	0.5	4.9	2.3
CV (%)	39%	39%	39%	63%	83%	94%	39%

T.C = Total count in Ur; eU = equivalent U (ppm), eTh = equivalent Th (ppm), K = K (%); μR/h = Microroentgen per hour, X = arithmetic mean, σ = standard deviation and CV (%) = coefficient of variability.

control on heat generation.

3.5. Environmental monitoring

3.5.1. Exposure rate

Natural gamma radiation at ground level is primarily generated by the radioactive decay of potassium-40, uranium, and thorium and their daughter products. Measurements of potassium, equivalent uranium, and equivalent thorium concentrations, typically obtained from gamma-ray spectrometry, provide a reliable means of quantifying environmental radiation exposure (Bücker & Rybach, 1996; Eisenbud & Gesell, 1997).

The ground-level exposure rate can be estimated from the apparent concentrations of p (K, %), (eU, ppm), and (eTh, ppm) following the formulation of the (IAEA, 2010):

$$\text{Exposure rate}\ (\mu\text{R}/\text{h}) = 1.505\,K(\%) + 0.653\,eU(\text{ppm}) + 0.287\,eTh(\text{ppm}) \tag{4}$$

3.5.2. Absorbed dose rate

The energy imparted by ionizing radiation to 1 g of material at a specific point is defined as the absorbed dose (D). The traditional unit of absorbed dose is the rad (radiation absorbed dose) (Sharma et al., 2018). Because different types of ionizing radiation produce varying biological effects in living tissues, a derived quantity known as the dose equivalent is used to assess potential biological impact. This quantity is expressed in the unit rem (roentgen equivalent man), where 1 rem represents the dose of any type of radiation that produces the same biological effect in humans.

The conversion from exposure rate to absorbed dose rate:

$$\text{D}\ (\text{mrem}/\text{year}) = 8.33 \times \text{E}\ (\mu\text{R}/\text{h}) \tag{5}$$

In recent years, radiation protection quantities have been increasingly expressed using the International System of Units (SI). The SI unit corresponding to the rem is the sievert (Sv), which measures equivalent dose:

$$1\ \text{Sv} = 100\ \text{rem} \tag{6}$$

Accordingly, the dose rate can be expressed in SI units as:

$$\text{D}\ (\text{mSv}/\text{year}) = 0.0833 \times \text{E}\ (\mu\text{R}/\text{h}) \tag{7}$$

3.6. Aeromagnetic data

3.6.1. Reduction to north magnetic pole (RTP)

The method of reduction to the pole (RTP) is used to remove this effect, so that the data appear as if observed at the pole, where the magnetic field is vertical. According to (Blakely, 1995), the field reduced to the pole at a fixed point above the measurement plane in frequency domain is given as:

$$\text{L}(\theta) = 1/[\sin(\text{I}_\alpha) - \text{i}\cos(\text{I})\cos(\text{D}+\theta)]^2, \text{if}\ (\text{I}_\alpha < \text{I}), \text{I}_\alpha = \text{I} \tag{8}$$

Where: **I** is the geomagnetic inclination; $\mathbf{I_\alpha}$ is the inclination for amplitude correction; **D** is the geomagnetic declination; **θ** is the wave number direction; and **i** is the imaginary component.

Reduction to the pole has an amplitude component (the sin term) and a phase component [the i cos (I). cos (D+θ) component]. An amplitude inclination of 90° causes only the phase component to be applied to the data (no amplitude correction) and the value of 0° causes phase and amplitude component to be applied over the entire range.

3.6.2. Calculation of power spectrum

The energy decay curve includes linear segments, with distinguishable slopes, that are attributed to the contributions in the bouguer data from the residual (shallower sources), as well as the regional (deep sources) lithologic and/or structural features. The presentation of the method depends on plotting the energy spectrum against frequency on a logarithmic scale. The plot shows straight-line segments, which decrease in slope with the increase of frequency. The slopes of the segments yield estimates of the average depths to gravity sources. The depth for each segment was calculated by introducing the slope of this segment through the following formula (Spector, 1975):

$$\text{h (depth)} = -\,\text{slope}/4\pi \tag{9}$$

3.6.3. Regional-residual separation

The RTP magnetic map, which is gridded before and contoured by using Oasis Montaj $^{\text{tm}}$ software package (version 6.4.2) is separated directly into regional and residual components. The low-pass (regional) magnetic map; it is defined as the filters which pass the long wavelengths and reject all wavelengths smaller than the cut-off wavenumber. The band-pass for the higher frequency (residual) magnetic map is defined as the filters which pass all smaller wavelengths and reject all long wavelengths greater than the cut-off wave number. This map represents actually the distribution of the magnetic field at a shallow depth.

3.6.4. First vertical derivative (FVD)

The FVD field map is often used to detect edges and geologic boundaries in data (Henderson & Zietz, 1949). The vertical derivative is commonly applied to RTP magnetic data to enhance the shallow geologic source in the data. Vertical derivative maps, usually the first or second vertical derivative, accentuate gradients along edges of shallow magnetic sources. Hence, they are used to locate edges of magnetic bodies and to emphasize sources at shallow depths (Dobrin & Savit, 1961).

3.6.5. Tilt derivative (TDR)

The TDR of magnetic anomaly field is a method for edge detection (Miller & Singh, 1994; Verduzco et al., 2004). It is calculated according to the following equation:

$$TDR = \tan^{-1}\left(\frac{\partial f/\partial z}{\sqrt{(\partial f/\partial x)^2 + (\partial f/\partial y)^2}}\right) \tag{10}$$

Where: ∂f/∂x, ∂f/∂y, and ∂f/∂z are the derivatives of the magnetic field in the x, y and z directions respectively.

The tilt derivative is similar to the phase component of the analytical signal and by the nature of tangent function, it uses ranges from $-\pi/2$ to $\pi/2$. In this way amplitudes of magnetic fieldstend to be equalized (Verduzco et al., 2004). The tilt derivative has values close to zero above edges of the causative bodies.

3.6.6. Euler deconvolution method (ED)

The ED technique is commonly used to estimate the locations of magnetic sources and to provide quantitative information on source parameters, including depth, dip, and susceptibility contrast (Mushayandebvu et al., 2001; Thompson, 1982). This method is based on solving Euler's homogeneity equation and requires the selection of an appropriate structural index (SI), which reflects the geometry of the causative source.

4. Results and discussion

4.1. Gamma ray spectrometry

4.1.1. Total-count (T.C) surface distribution map

A comprehensive examination of the surface total-count radioactivity (T.C, Ur) distribution map for the study area (Fig. 2a) reveals that the Pliocene deposits, Thebes Group, Esna Formation, Quseir Formation, Metavolcanics, Taref Formation, Dakhla Formation, and Tarawan

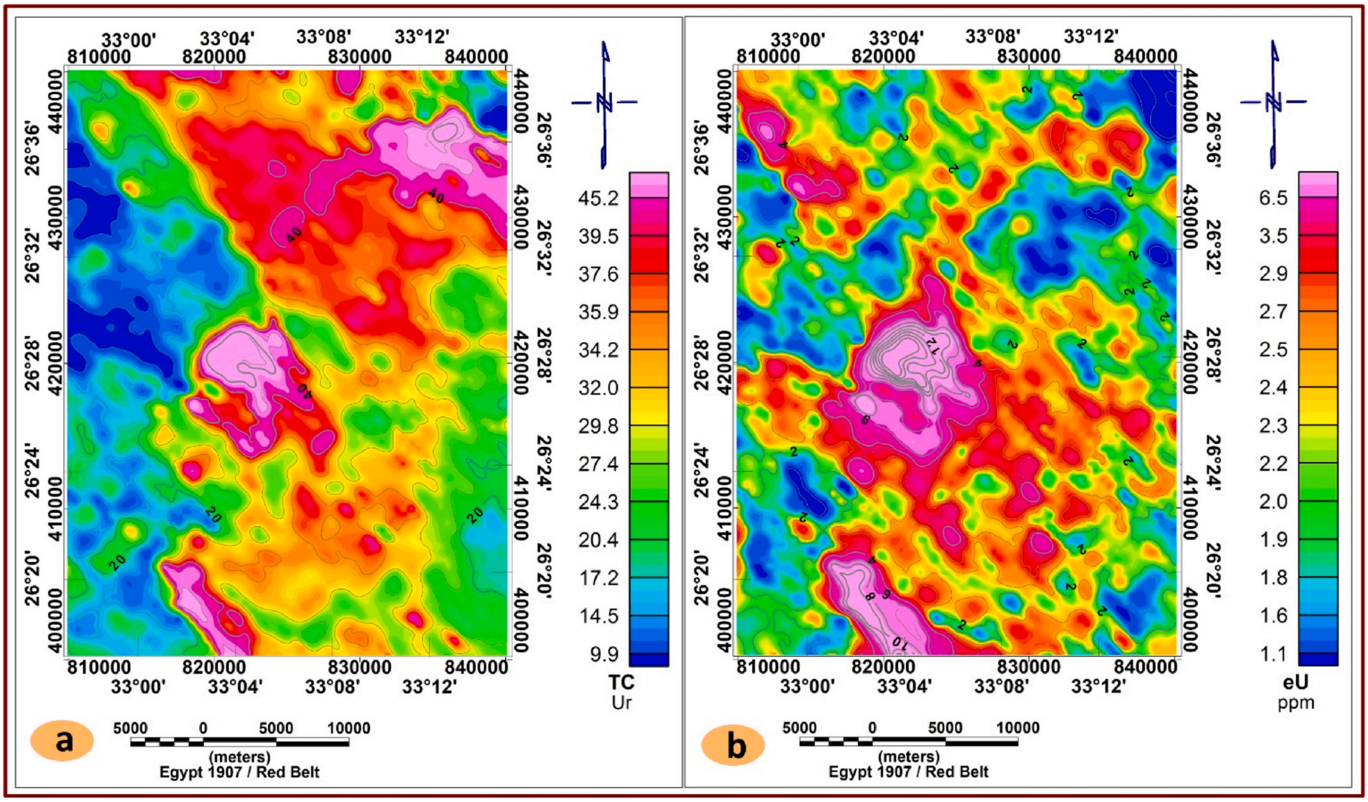

Fig. 2. a) Filled color contour map of total-count radioactivity (TC); **b**) Filled color contour map of Equivalent uranium radioactivity (eU).

Formation generally exhibit values below 30 Ur. These lower readings follow distinct structural trends oriented northwest–southeast (NW-SE) and northeast–southwest (NE-SW). In contrast, the map highlights pronounced anomalies with values reaching up to 45 Ur. These

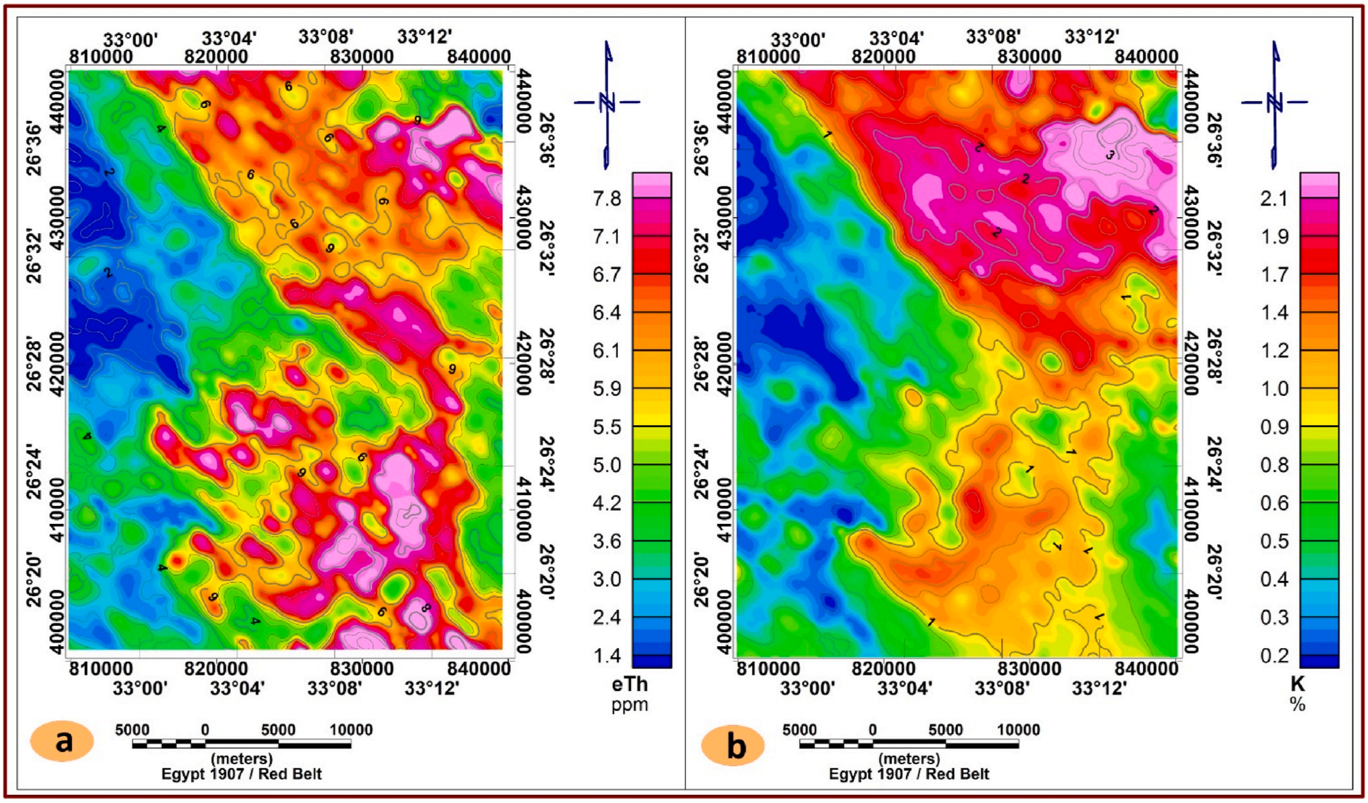

Fig. 3. a) Filled color contour map of eTh (ppm); **b**) Filled color contour map of K radioactivity (%).

anomalies are represented by red and magenta zones and are concentrated over the Duwi Formation, Younger granites, fangelomerate, and Wadi deposits. The elevated amplitudes of these anomalies mark them as significant exploration targets. The dominant orientation of these high-radioactivity zones is NW–SE.

4.1.2. Equivalent uranium (eU) surface distribution map

The eU (ppm) distribution map (Fig. 2b) can be divided into two distinct levels. The first level is characterized by elevated uranium concentrations, reaching up to 6.5 ppm, and extends across the study area with dominant NW-SE and NE-SW trends. These high values are primarily associated with the Duwi Formation, Tarawan Formation, Dakhla Formation, and Quseir Formation. The second level represents lower uranium concentrations, generally less than 2.5 ppm. This zone is linked to the Taref Formation, Fangelomerate, Wadi deposits, Thebes group, younger granites, Esna Formation, and metavolcanics.

4.1.3. Equivalent thorium (eTh) surface distribution map

The predictive map of eTh concentrations across the study area (Fig. 3a) reveals moderately high values ranging from 5.5 to 7.8 ppm. Elevated thorium levels are concentrated in the Younger Granites, Quseir Formation, Wadi deposits, and Fangelomerate. Conversely, lower thorium concentrations, ranging between 1.4 and 5.5 ppm, are associated with the Taref Formation, Duwi Formation, metavolcanics, Dakhla Formation, Tarawan Formation, Pliocene deposits, Thebes Group, and Esna Formation. These zones represent areas of reduced thorium enrichment compared to the anomalous high-value regions.

4.1.4. Potassium (K) surface distribution map

The K contour map (Fig. 3b) reveals two distinct concentration levels. The first level is characterized by relatively low K radiation values and is distributed across the western, central, and eastern sectors of the study area. These low concentrations are primarily associated with the Quseir Formation, Duwi Formation, Tarawan Formation, Dakhla Formation, Pliocene deposits, Thebes Group, and Esna Formation. The dominant structural trends of these zones are oriented northwest-southeast (NW-SE) and northeast-southwest (NE-SW). The second level is defined by relatively high potassium radiation, with concentrations reaching up to 2.1%. This zone is mainly linked to the younger granites, Fangelomerate, metavolcanics, Wadi deposits, and Taref Formation, also following NW-SE and NE-SW structural orientations.

4.1.5. Composite radioelement map

The composite radioelement map (Fig. 4a), which integrates eU in red, K in green, and equivalent eTh in blue, shows a strong spatial correlation with the geological map (Fig. 1b). High radioelement concentrations, represented by bright colors, are primarily associated with younger granitic rocks. These rocks are typically characterized by a strong radiometric response, are clearly expressed on the composite radioelement image, and can be readily distinguished from lithologies with low radioactivity.

Areas exhibiting anomalously high background concentrations of eU, eTh, and K display a pronounced spatial correspondence with these granitic units. In contrast, low concentrations of eU, eTh, and K appear as dark regions on the map (Fig. 4a), indicating a close association with sedimentary deposits. These zones show a sharp color contrast relative to the brightly colored granitic rocks, reflecting significant differences in radioelement content among the various lithological units.

4.1.6. Radiogenic heat production (RHP)

The RHP reflects the contribution of radioactive elements, primarily U, Th, and K, to the internal heat budget of the Earth's crust. The spatial distribution observed in the study area indicates significant lithological control on heat generation. The RHP values (more than 0.71μW/m^3) (Fig. 4b) recorded in the northeastern and southern-central sectors are mainly associated with crystalline and coarse-grained lithologies, such as younger granites and metavolcanic rocks. These rock types are

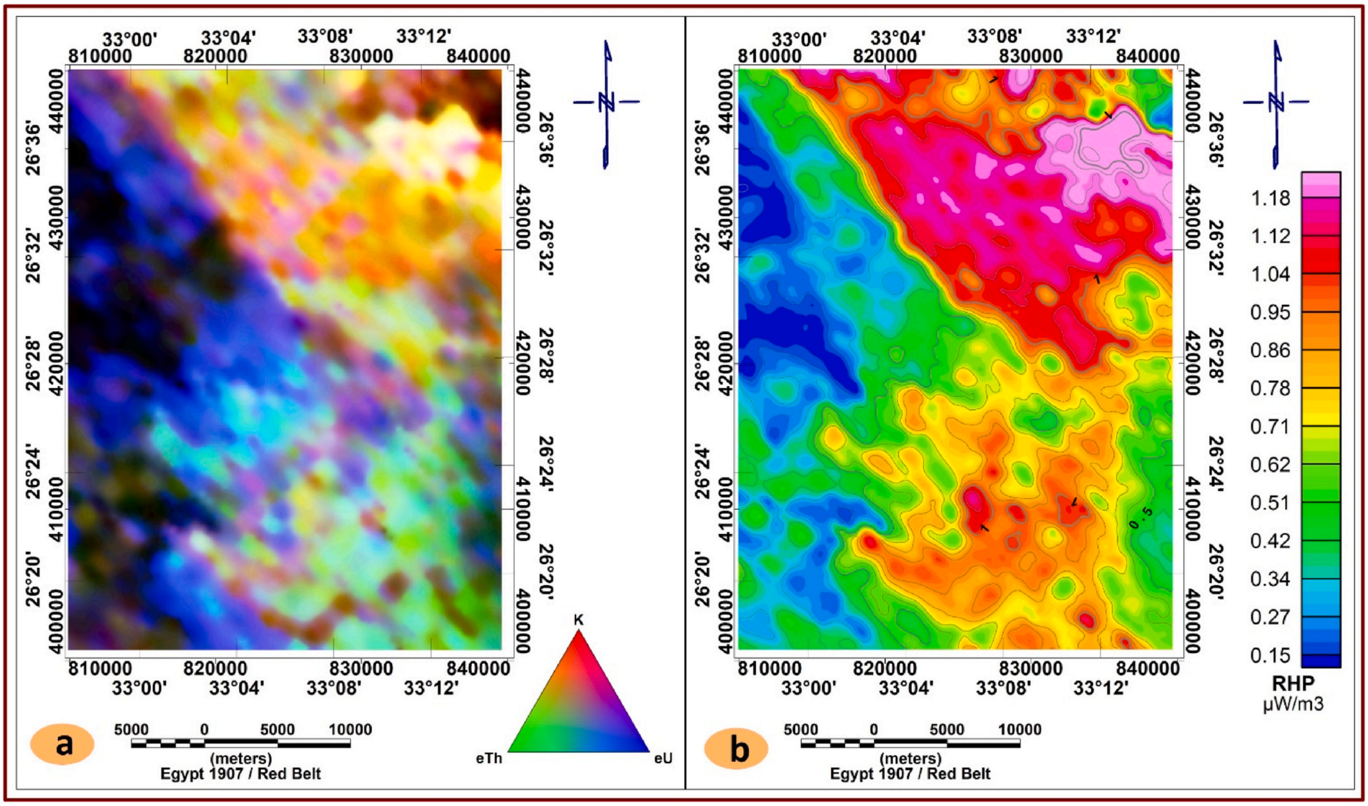

Fig. 4. **a)** Radio-element composite image map; **b)** Radiogenic heat production distribution map of the study area.

typically enriched in heat-producing radioactive elements, explaining their elevated heat production. The presence of Fangelomerate and Wadi deposits within this category suggests sedimentary reworking of radioactive mineral-rich source rocks. Conversely, the western part of the study area is dominated by sedimentary formations with comparatively low concentrations of radioactive elements, resulting in lower radiogenic heat production (less than 0.71μW/m^3). Formations such as Quseir, Duwi, Tarawan, Dakhla, and Esna consist largely of fine-grained clastic or carbonate rocks, which generally contain fewer heat-producing minerals. Overall, the radiogenic heat production map (Fig. 4b) highlights the influence of geological composition and tectonic evolution on the thermal structure of the crust. These variations are crucial for understanding regional geothermal potential, crustal heat flow, and the thermal maturation of sedimentary basins.

4.2. Statistical analysis

Based on the geological map of the study area, statistical analysis was subsequently applied to seven variables (TC, eU, eTh, K, eU/eTh, eU/K, and eTh/K) within each identified rock unit. The statistical results for the four primary variables and the three derived ratios across the different lithological units are summarized in Table 2 and interpreted in the discussion section.

5. Interpretation and discussion

5.1. Relationship between radioactivity and lithology

According to the radiometric levels estimated from the lithologic units, the relationship between the radioactivity of the area and the mapped surface geology has been interpreted, as shown in Fig. 1b (the comprehensive geological map). Based on an analysis of the spectrometric maps (Figs. 2 and 3) it can be observed that the study area often has lower radiometric levels when compared to the geologic rock units.

5.1.1. Quaternary rocks

The coefficient of variability (CV %) less than 100% characterises the Quaternary sedimentary rocks. So, the rock units tend to normality in their distribution. The highest U concentrations exists over the Fangelomerate with eU values that ranged from 1.39 to 3.11 ppm, a mean of 2.29 ppm and coefficient of variability 15%, the K values range from 0.97 to 2.3% with a mean of 1.67% and coefficient of variability of 19%, and the eTh values differ from 4.88 to 8.17 ppm with a mean of 6.54 ppm and coefficient of variability of 9%. Statistical analysis clearly shows that the wadi deposits has low radiometric values with eU values ranging from 0.7 to 7.79 ppm and a mean of 2.28 ppm, coefficient of variability 37%, the K values range from 0.14 to 2.73% with a mean of 1.51% and coefficient of variability of 38%, and the eTh values are differing from 0.98 to 9.76 ppm with a mean of 5.78 ppm and coefficient of variability of 23%.

5.1.2. Tertiary rocks

The coefficient of variability (CV %) of Pliocene deposits less than 100%, which reflects that the rock units tend to normality in their distribution. The high U concentrations of these rocks are recorded over Pliocene deposits varying in the eU values ranging from 0.49 to 16.01 ppm with a mean of 2.75 ppm and coefficient of variability 77%, the K values range from 0.13 to 1.8% with a mean of 0.46% and coefficient of variability of 39%, and the eTh values are varying from 0.93 to 7.06 ppm with a mean of 3.12 ppm and coefficient of variability of 27%.

The statistical parameters derived from the radiometric data show that all coefficient of variation (CV %) values of Thebes group is below 100%, indicating that the measured variables display a tendency toward normal distribution. The eU concentrations range from 0.88 to 7.55 ppm, with a mean of 2.06 ppm, yielding a coefficient of variability of 53%, which reflects moderate variability within the dataset. The eTh exhibits a narrower spread, varying from 0.82 to 5.52 ppm, including with a mean values 1.65 ppm, and shows a coefficient of variability of 39%, suggesting relatively stable thorium distribution. The K concentrations lie between 0.09 and 0.65%, with a mean of 0.24%, and a coefficient of variability of 37%, indicating the lowest variability among the measured variables.

The radiometric data of the Esna Formation reveal CV % well below 100%, indicating that the distribution of the measured parameters tends toward normality. The eU concentrations range from 21 to 2.50 ppm, with a mean of values of 1.71 ppm, and exhibit a CV of 28%, reflecting relatively low variability. The eTh values vary between 0.36 and 2.11 ppm with median 1.38 ppm, and display a CV of 26%, suggesting a similarly stable distribution. The K contents lie within a narrow interval of 0.17 to 0.31%, with a mean of values of 0.23%, and present the lowest variability, with a CV of 22%. Collectively, these parameters indicate that the Esna Formation exhibits limited geochemical dispersion across its radiometric constituents.

The Tarawan Formation exhibits generally low radiometric signatures across its measured constituents. The eU concentrations vary between 2.42 and 8.36 ppm, with an average value of 4.22 ppm and a coefficient of variation of 40%, indicating moderate variability within the U distribution. The eTh shows a narrower range, spanning from 1.95 to 4.08 ppm, with a mean of 3.19 ppm and a comparatively low CV of 17%, reflecting a more uniform Th content. The K% concentrations extend from 0.31 to 0.73%, averaging 0.50%, and present a CV of 26%, suggesting modest fluctuation in potassium levels.

5.1.3. Cretaceous rocks

The Dakhla Formation exhibits elevated concentrations of eU, ranging from 1.36 to 14.82 ppm, with an average value of 4.11 ppm and a CV of 83%. The eTh concentrations vary between 1.91 and 4.08 ppm, averaging 3.3 ppm, with a coefficient of variability of 15%. The K% content within this formation ranges from 0.37% to 0.52%, with a mean value of 0.45% and a coefficient of variability of 10%.

The Duwi Formation is characterized by high eU concentrations, ranging from 1.94 to 20.34 ppm, with a mean value of 9.15 ppm and a CV of 54%. The eTh concentrations range from 2.37 to 7.99 ppm, averaging 4.84 ppm, with a CV of 21%. The K% content in this formation varies between 0.18% and 1.03%, with a mean of 0.57% and a CV of 27%.

The eU concentrations in the Quseir Formation are varying from 0.88 to 11.71 ppm. The mean value is 2.93 ppm, and the CV is 44%. The concentrations of eTh vary from 2.97 to 12.59 ppm, with an average of 6.33 ppm and a CV of 21%. With a coefficient of variability of 32% and a range of 0.17% to 2.1%, the K% concentration of this formation is 0.98% on average.

In the Taref Formation, the eU concentrations range from 1.41 to 3.31 ppm. The CV is 15%, while the mean value is 2.3 ppm. With an average of 5.12 ppm and a CV of 24%, the eTh values range from 2.99 to 8.66 ppm. The K% concentration of this formation is 1.07% on average, with a range of 0.48% to 2.31% and a coefficient of variability of 44%.

5.1.4. Basement rocks

The younger granites exhibit low to moderate radiometric signatures, with equivalent uranium (eU) concentrations ranging from 0.6 to 3.2 ppm, a mean of 1.9 ppm, and a CV of 37%. The eTh levels vary between 2.5 and 10.2 ppm, averaging 6.5 ppm, with a CV of 21%. The K % content ranges from 0.4% to 2.7%, with a mean value of 1.1% and a CV of 31%. These values indicate that the younger granites are relatively enriched in Th compared to U, reflecting a radiometric signature typical of felsic granitic compositions with moderate K content.

The metavolcanic rocks display low to moderate radiometric signatures, with eU concentrations ranging from 0.02 to 3.62 ppm, a mean of 1.61 ppm, and a CV of 55%. The eTh concentrations range from 1.4 to 9.27 ppm, averaging 4.66 ppm, with a CV of 37%. The K% content varies between 0.39% and 3.49%, with a mean of 1.57% and a CV of 43%.

Table (2)
Summary of the statistical treatments of gamma-ray spectrometric data.

Rocks	Age	Radio.	NO.	Min	Max	Range	(X)	(σ)	(CV%)	x+σ	x+2σ	x+3σ
Fangelomerate	**Quaternary**	TC	97	28.01	45.09	17.08	36.30	3.87	11%	40.16	44.03	47.90
		eU		1.39	3.11	1.72	2.29	0.34	15%	2.63	2.97	3.31
		eTh		4.88	8.17	3.29	6.54	0.59	9%	7.13	7.71	8.30
		K		0.97	2.30	1.33	1.67	0.32	19%	1.99	2.31	2.63
		eU_eTh		0.24	0.56	0.32	0.35	0.06	17%	0.41	0.47	0.54
		eU_K		0.89	3.19	2.30	1.45	0.50	35%	1.96	2.46	2.96
Wadi Deposits		TC	1367	8.82	53.16	44.34	33.52	7.57	23%	41.09	48.66	56.23
		eU		0.70	8.49	7.79	2.28	0.84	37%	3.13	3.97	4.81
		eTh		0.98	9.76	8.78	5.78	1.34	23%	7.12	8.46	9.80
		K		0.14	2.73	2.59	1.51	0.57	38%	2.08	2.65	3.23
		eU_eTh		0.12	2.15	2.03	0.43	0.25	57%	0.68	0.93	1.17
		eU_K		0.34	13.48	13.14	2.12	2.04	96%	4.16	6.20	8.24
Pliocene Deposits	**Tertiary**	TC	1174	9.10	68.90	59.80	19.59	8.51	43%	28.10	36.61	45.12
		eU		0.49	16.01	15.52	2.75	2.11	77%	4.85	6.96	9.06
		eTh		0.93	7.06	6.13	3.12	0.85	27%	3.97	4.81	5.66
		K		0.13	1.80	1.67	0.46	0.18	39%	0.64	0.83	1.01
		eU_eTh		0.14	3.82	3.68	0.88	0.52	59%	1.40	1.92	2.44
		eU_K		0.92	31.94	31.02	6.52	4.88	75%	11.40	16.29	21.17
Thebes Group		TC	286	7.24	38.12	30.88	12.10	4.47	37%	16.57	21.05	25.52
		eU		0.88	7.55	6.67	2.06	1.08	53%	3.15	4.23	5.31
		eTh		0.82	5.52	4.70	1.65	0.64	39%	2.29	2.93	3.57
		K		0.10	0.65	0.55	0.24	0.09	37%	0.33	0.42	0.51
		eU_eTh		0.47	3.14	2.67	1.27	0.41	32%	1.68	2.08	2.49
		eU_K		2.65	25.06	22.41	8.91	3.86	43%	12.76	16.62	20.47
Esna Fm.		TC	10	9.26	14.68	5.42	10.25	1.67	16%	11.92	13.59	15.26
		eU		1.21	2.50	1.29	1.71	0.48	28%	2.19	2.67	3.15
		eTh		0.72	2.11	1.39	1.38	0.36	26%	1.74	2.11	2.47
		K		0.17	0.31	0.14	0.23	0.05	22%	0.28	0.34	0.39
		eU_eTh		0.81	3.33	2.52	1.36	0.76	56%	2.12	2.87	3.63
		eU_K		4.19	8.14	3.95	6.04	1.41	23%	7.46	8.87	10.29
Tarawan Fm.		TC	24	14.66	38.20	23.54	23.69	6.78	29%	30.47	37.25	44.03
		eU		2.42	8.36	5.94	4.22	1.69	40%	5.91	7.59	9.28
		eTh		1.95	4.08	2.13	3.19	0.54	17%	3.73	4.27	4.80
		K		0.31	0.73	0.42	0.50	0.13	26%	0.63	0.76	0.88
		eU_eTh		0.87	2.43	1.56	1.31	0.41	32%	1.72	2.13	2.54
		eU_K		3.92	21.01	17.09	8.96	4.11	46%	13.06	17.17	21.28
Dakhla Fm.	**Cretacous**	TC	34	11.85	62.13	50.28	24.25	12.53	52%	36.77	49.30	61.83
		eU		1.36	14.82	13.46	4.11	3.41	83%	7.52	10.93	14.35
		eTh		1.91	4.08	2.17	3.30	0.50	15%	3.80	4.30	4.79
		K		0.37	0.52	0.15	0.45	0.05	10%	0.50	0.55	0.60
		eU_eTh		0.35	4.35	4.00	1.19	0.89	75%	2.09	2.98	3.87
		eU_K		2.97	29.93	26.96	9.02	7.24	80%	16.26	23.50	30.75
Duwi Fm.		TC	169	18.71	86.80	68.09	45.56	16.54	36%	62.10	78.64	95.18
		eU		1.94	20.34	18.40	9.15	4.95	54%	14.10	19.06	24.01
		eTh		2.37	7.99	5.62	4.84	1.04	21%	5.88	6.92	7.96
		K		0.18	1.03	0.85	0.57	0.15	27%	0.73	0.88	1.03
		eU_eTh		0.33	5.86	5.53	1.98	1.20	60%	3.18	4.38	5.58
		eU_K		1.99	50.80	48.81	18.01	11.76	65%	29.77	41.53	53.29
Quseir Fm.		TC	1374	14.53	52.91	38.38	30.78	5.85	19%	36.63	42.48	48.33
		eU		0.88	11.71	10.83	2.93	1.28	44%	4.22	5.50	6.79
		eTh		2.97	12.59	9.62	6.33	1.32	21%	7.65	8.97	10.29
		K		0.17	2.10	1.93	0.98	0.31	32%	1.30	1.61	1.92
		eU_eTh		0.17	2.23	2.06	0.49	0.26	53%	0.74	1.00	1.26
		eU_K		0.70	26.14	25.44	3.46	2.58	75%	6.04	8.63	11.21
Taref Fm.		TC	118	18.50	48.59	30.09	27.38	7.13	26%	34.51	41.63	48.76
		eU		1.41	3.31	1.90	2.30	0.35	15%	2.65	3.01	3.36
		eTh		2.99	8.66	5.67	5.12	1.21	24%	6.33	7.54	8.76
		K		0.48	2.31	1.83	1.07	0.47	44%	1.54	2.02	2.49
		eU_eTh		0.22	0.77	0.55	0.47	0.12	25%	0.59	0.71	0.82
		eU_K		0.71	6.67	5.96	2.53	1.10	43%	3.63	4.73	5.83
Younger Granites	**Basement**	TC	222	13.7	67.1	53.4	39.2	10.2	26%	49.4	59.6	69.8
		eU		0.6	3.2	2.7	1.9	0.5	27%	2.5	3.0	3.5
		eTh		2.5	10.2	7.8	6.5	1.4	21%	7.9	9.3	10.7
		K		0.7	3.6	2.9	2.0	0.6	31%	2.7	3.3	3.9
		eU_eTh		0.1	0.5	0.4	0.3	0.1	24%	0.4	0.4	0.5
		eU_K		0.4	2.7	2.3	1.1	0.5	44%	1.5	2.0	2.4
Metavolcanics		TC	152	5.02	62.83	57.81	30.12	12.71	42%	42.83	55.55	68.26
		eU		0.02	3.62	3.64	1.61	0.89	55%	2.50	3.39	4.28
		eTh		1.40	9.27	7.87	4.66	1.74	37%	6.41	8.15	9.89
		K		0.39	3.49	3.10	1.57	0.68	43%	2.26	2.94	3.63
		eU_eTh		0.01	0.63	0.62	0.33	0.12	37%	0.45	0.57	0.68
		eU_K		0.00	1.69	1.69	0.99	0.34	35%	1.33	1.67	2.01

Min = minimum, Max = maximum, X = mean, σ = Standard Deviation, CV % = Coefficient of Variability in % and No= Number of readings over every lithologic unit, and (TC) = Total-count**.**

These data suggest that the metavolcanics are relatively enriched in Th compared to U, and the moderate K levels indicate a diverse mineralogical composition, reflecting both felsic and mafic contributions.

5.2. Environmental monitoring

5.2.1. Exposure rate

The RER map reveals three main levels of radiation intensity (Table 3). The first level represents relatively high radiation values, which are mainly associated with granitic rocks and the Duwi Formation (Fig. 5). These values range from 6 to 8 μR/h and are represented by red to magenta colors on the RER map. The second, intermediate radiation level is primarily correlated with the Fanglomerate, Wadi deposits, Dakhla Formation, Quseir Formation, and metavolcanic rocks. Exposure rates within this category range from 3 to 6 μR/h and are depicted by green, yellow, and orange colors on the RER map. The third and lowest radiation level in the study area is mainly associated with Pliocene deposits, the Thebes Group, Esna Formation, and Taref Formation. Exposure rates in this group range from 1.7 to 3 μR/h and are shown in pale blue on the RER map (Fig. 6a).

5.2.2. Dose rate

The RDR analysis of the study area (Fig. 5) exhibits spatial patterns that closely correspond to those observed in the RER map (Fig. 5a), reflecting their common derivation from the same radioelement distributions. Although both maps delineate identical spatial features, they differ in magnitude and units because the RDR is expressed in standard dose units that more directly reflect potential biological effects. Accordingly, Table 3 and RDR map (Fig. 6b) identifies three principal radiation dose levels within the study area: a high dose level ranging from 0.50 to 0.69 mSv/y, an intermediate level ranging from 0.25 to 0.50 mSv/y, and a low dose level ranging from 0.15 to 0.25 mSv/y.

The spatial distribution of these dose levels is strongly controlled by lithology. Higher dose rates are predominantly associated with granitic rocks and other lithological units enriched in uranium, thorium, and potassium, reflecting their elevated concentrations of naturally occurring radioactive materials. Intermediate dose rates correspond mainly to mixed sedimentary and volcanic units, where radioelement concentrations are moderate.

The lowest dose rates are generally confined to younger sedimentary deposits characterized by low natural radioactivity, indicating limited radiological influence from terrestrial gamma radiation. International radiation protection guidelines established by scientific and medical authorities, including the International Atomic Energy Agency (IAEA, 2010), provide reference levels for evaluating potential radiological risks. According to these guidelines, the annual radiation dose equivalent (RDE) is unlikely to exceed 1.0 mSv/y under normal natural background conditions, and no specific control measures are required within this range. For annual doses between 1.0 and 6.0 mSv/y, a formal dose assessment program is recommended, employing either workplace or individual monitoring. If annual doses are expected to exceed 6.0 mSv/y, individual monitoring becomes mandatory to ensure adequate radiation protection.

In the context of the present study, the estimated mean annual natural radiation dose rates from terrestrial gamma radiation range between 0.15 and 0.69 mSv/y (Fig. 6b). These values lie well below the internationally recommended limits and fall within the range considered safe for continuous whole-body external exposure. Consequently, the radiological environment of the study area does not pose a significant health risk to the population, and no additional radiation protection measures are required under current conditions.

5.3. Magnetic data interpretation

The Oasis Montaj ^{tm} software package (version 6.4.2) was used in the analysis and contouring of data. The main target of this study is to identify the subsurface structure framework and related shear zones, in addition to, delineate the sedimentary cover basins of the study area.

5.3.1. Total magnetic intensity map (TMI)

Inspections of the TMI map (Fig. 7a) reveal that, the northeastern, northwestern, southeastern and southwestern parts of the study area are occupied by low magnetic values (less than −20 nT). While the northern, eastern, western and central parts of the area are occupied by high and moderate magnetic values ranging from −20 nT to >160 nT.

5.3.2. Reduced to the northern magnetic pole map (RTP)

The RTP magnetic anomaly map of the study area (Fig. 7b) can be subdivided into three distinct magnetic zones based on anomaly amplitude and spatial frequency. The first zone is characterized by high-amplitude anomalies with dense magnetic lineation patterns, exhibiting values ranging from approximately 125 nT to more than 220 nT. This zone is mainly distributed in the northwestern, southwestern, eastern, and central parts of the study area and is interpreted to reflect the presence of shallow, highly magnetized source bodies, likely associated with crystalline basement rocks or mafic to intermediate intrusions. The second zone comprises anomalies of intermediate amplitude, with values ranging from about −15 to 125 nT. It occurs in parts of the northwestern, southern, and central sectors of the area. This zone likely represents regions with moderate magnetic susceptibility, possibly related to basement rocks at greater depths or mixed lithologies with varying magnetic properties. The third zone is characterized by low to very low magnetic anomalies, with values less than −15 nT. This zone occupies the northern, northeastern, western, and southeastern sectors of the study area and is interpreted as indicating weakly magnetized rocks or areas where the magnetic basement is deeply buried beneath thick non-magnetic sedimentary cover.

Table (3)

Statistical calculations and frequency histogram of exposure rate (μR/h) and dose rates (mSv/y) for each rock units.

Rock units	Exposure rate (μR/h)				Dose Rate (mSv/y)			
	Min.	Max.	Mean	Standard deviation	Min.	Max.	Mean	Standard deviation
Fangelomerate	4.49	7.12	5.88	0.56	0.37	0.59	0.49	0.05
Wadi deposits	1.54	8.59	5.42	1.16	0.13	0.72	0.45	0.10
Pliocene deposits	1.46	12.41	3.38	1.55	0.12	1.03	0.28	0.13
Thebes group	1.12	7.3	2.18	0.93	0.09	0.61	0.18	0.08
Esna Fm.	1.5	2.7	1.86	0.37	0.13	0.23	0.16	0.03
Tarawan Fm.	2.76	7.05	4.42	1.22	0.23	0.59	0.36	0.10
Dakhla Fm.	2.14	11.41	4.31	2.31	0.18	0.95	0.36	0.19
Duwi Fm.	3.32	15.44	8.22	3.12	0.27	1.29	0.69	0.25
Quseir Fm.	2.34	9.83	5.12	0.98	0.20	0.82	0.43	0.08
Taref Fm.	3.24	7.8	4.58	0.98	0.26	0.64	0.38	0.09
Younger granites	2.44	10.24	6.21	1.53	0.20	0.85	0.52	0.13
Metavolcanics	1.03	10.01	4.76	2.00	0.09	0.83	0.40	0.17

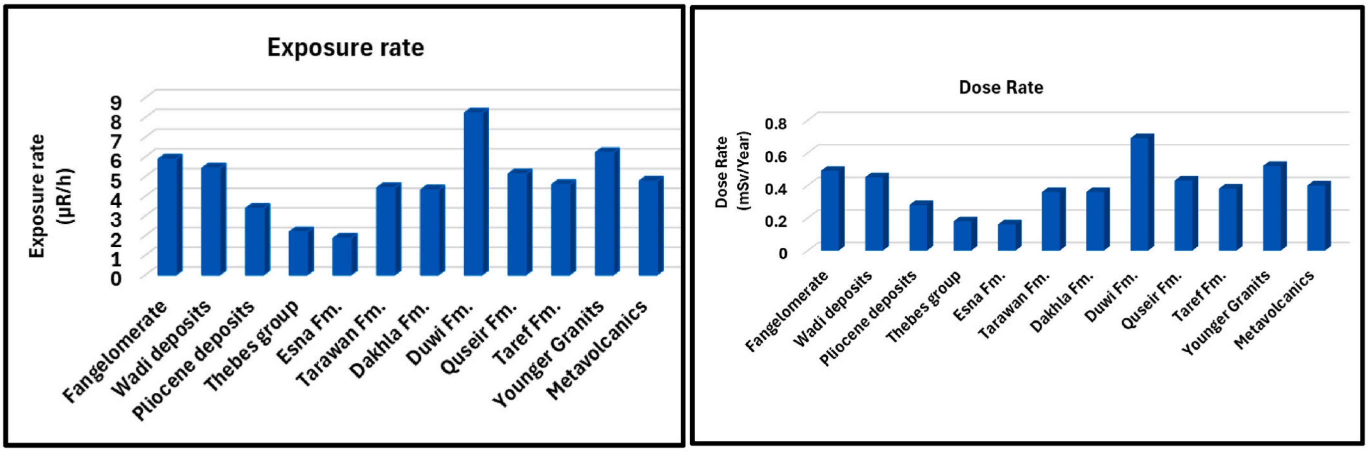

Fig. 5. Frequency histogram of exposure rate (μR/h) and dose rates (mSv/y) for each rock units.

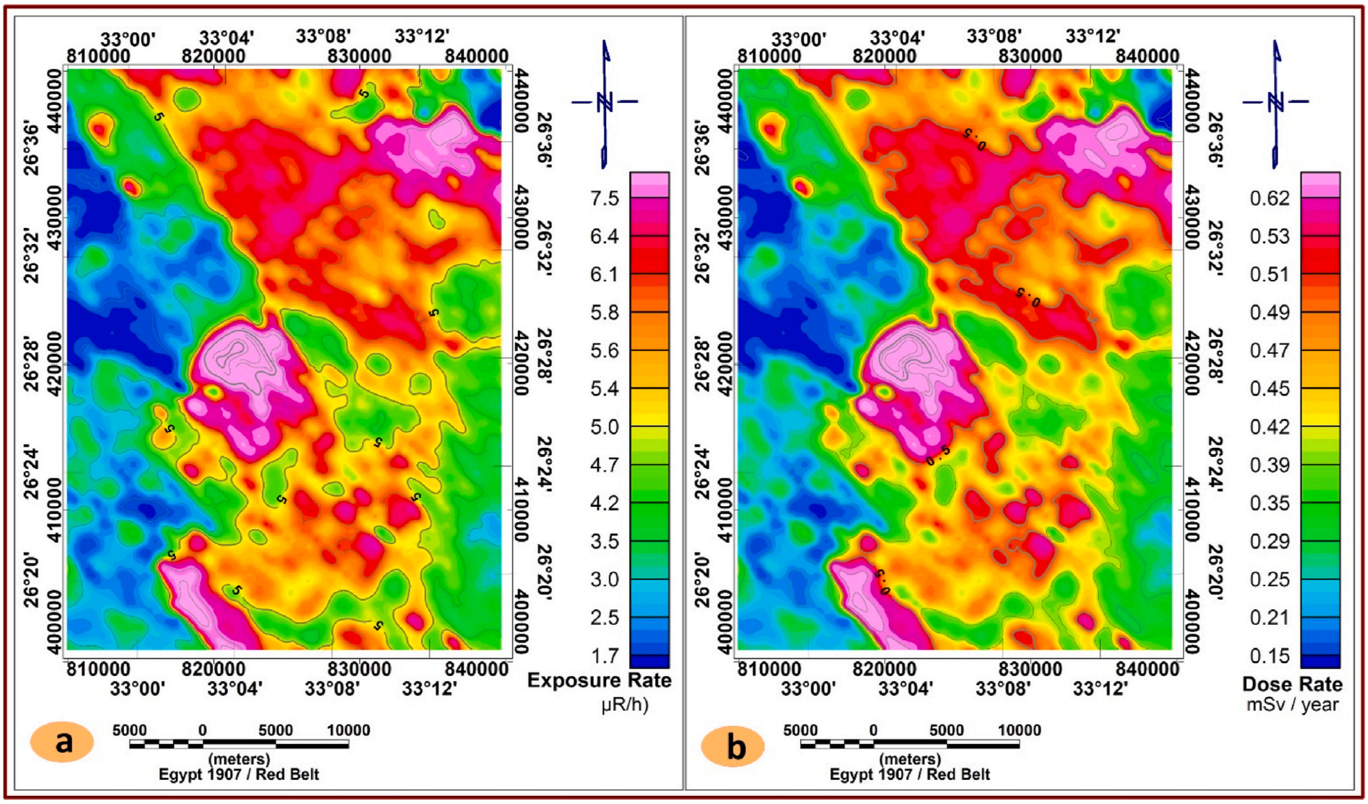

Fig. 6. **a**) Filled Color Map of Radiation Exposure Rate Map; **b**) Filled Color Map of Radiation Dose Rate.

5.3.3. *Radially averaged power spectrum*

Power spectrum analysis (Fig. 8) was applied to the reduced-to-the-pole (RTP) magnetic data to estimate the average depths of the regional and residual magnetic sources. The low-frequency components, representing deep-seated magnetic sources, range from 0.01 to 0.47 cycles per grid unit, whereas the high-frequency components, associated with shallow or near-surface sources, range from 0.47 to 1.9 cycles per grid unit. Interpretation of the power spectrum indicates the presence of two principal source interfaces at average depths of approximately 1.5 km and 0.5 km below the measurement level, corresponding to the regional and residual magnetic components, respectively.

5.3.4. *Regional and residual maps*

Examination of the regional (low-pass filtered) magnetic component map (Fig. 9a) reveals two main anomaly patterns. Negative magnetic anomalies, characterized by values less than zero, dominate the northern, northeastern, western, and southeastern parts of the study area. In contrast, positive magnetic anomalies are concentrated in the northwestern, southwestern, eastern, and central sectors, reflecting regions influenced by deeper and more strongly magnetized sources. Analysis of the residual (high-pass filtered) magnetic component map (Fig. 9b) indicates that several anomalies observed in the residual field are absent or significantly subdued in the regional magnetic map, particularly in the northern and northeastern parts of the area. These residual anomalies are attributed to shallow, near-surface magnetic sources and likely reflect localized lithological variations, minor intrusions, or structural features superimposed on the deeper regional magnetic field.

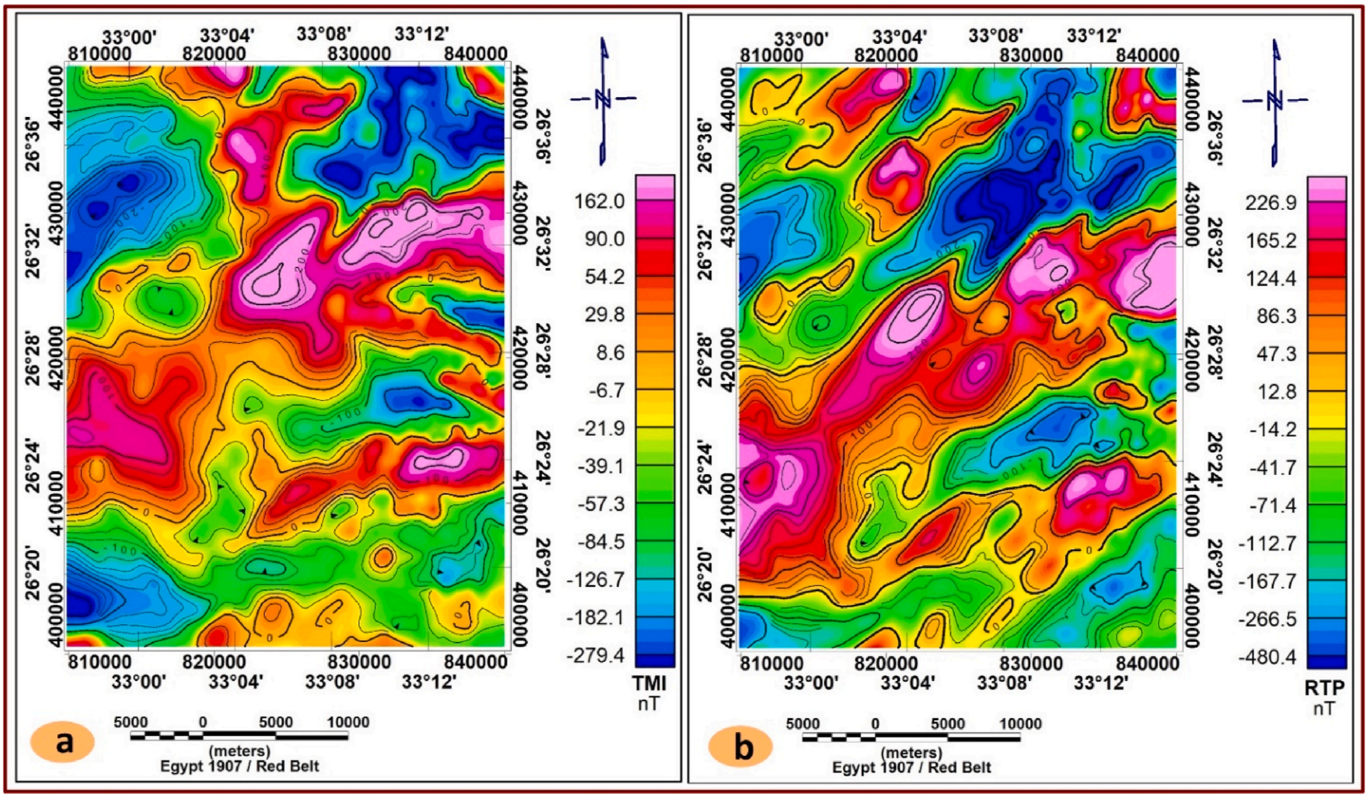

Fig. 7. **a**) Total magnetic intensity (TMI) map; and **b**) The reduced to the northern magnetic Pole (RTP) map of the study area.

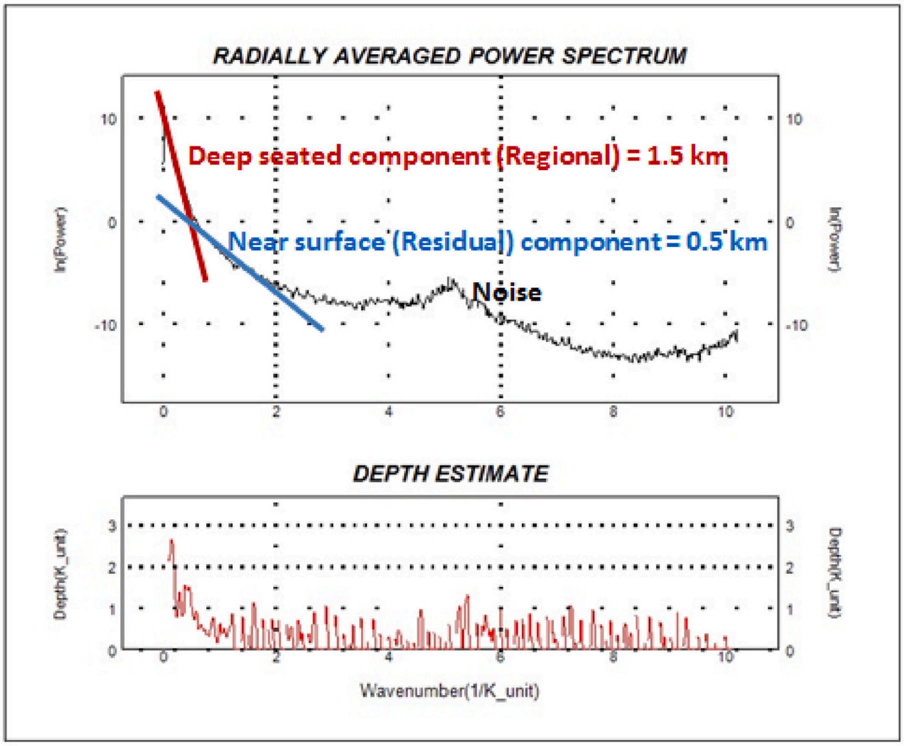

Fig. 8. Radially averaged power spectrum of the study area.

5.3.5. *First vertical derivative (FVD)*

The application of this technique aims to enhance and simplify the interpretation of the RTP magnetic data. The FVD accentuates shallow geological sources and sharpens the boundaries of magnetic bodies by amplifying short-wavelength anomalies. Both the first and second vertical derivatives are effective in highlighting near-surface sources and delineating zones of rapid magnetic gradient change around the edges of these sources (Dobrin & Savit, 1961). The FVD map (Fig. 10a) clearly

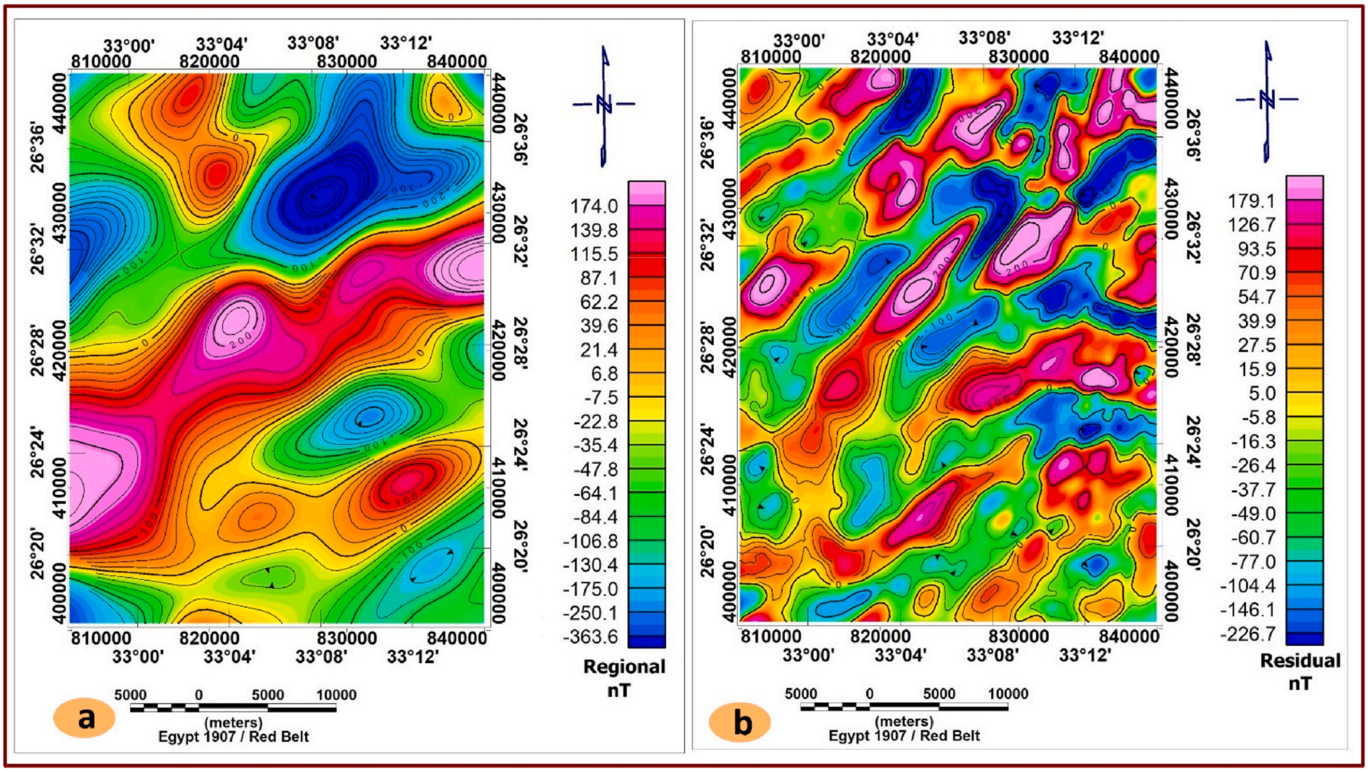

Fig. 9. a) Regional magnetic map; and **b)** Residual magnetic map of the study area.

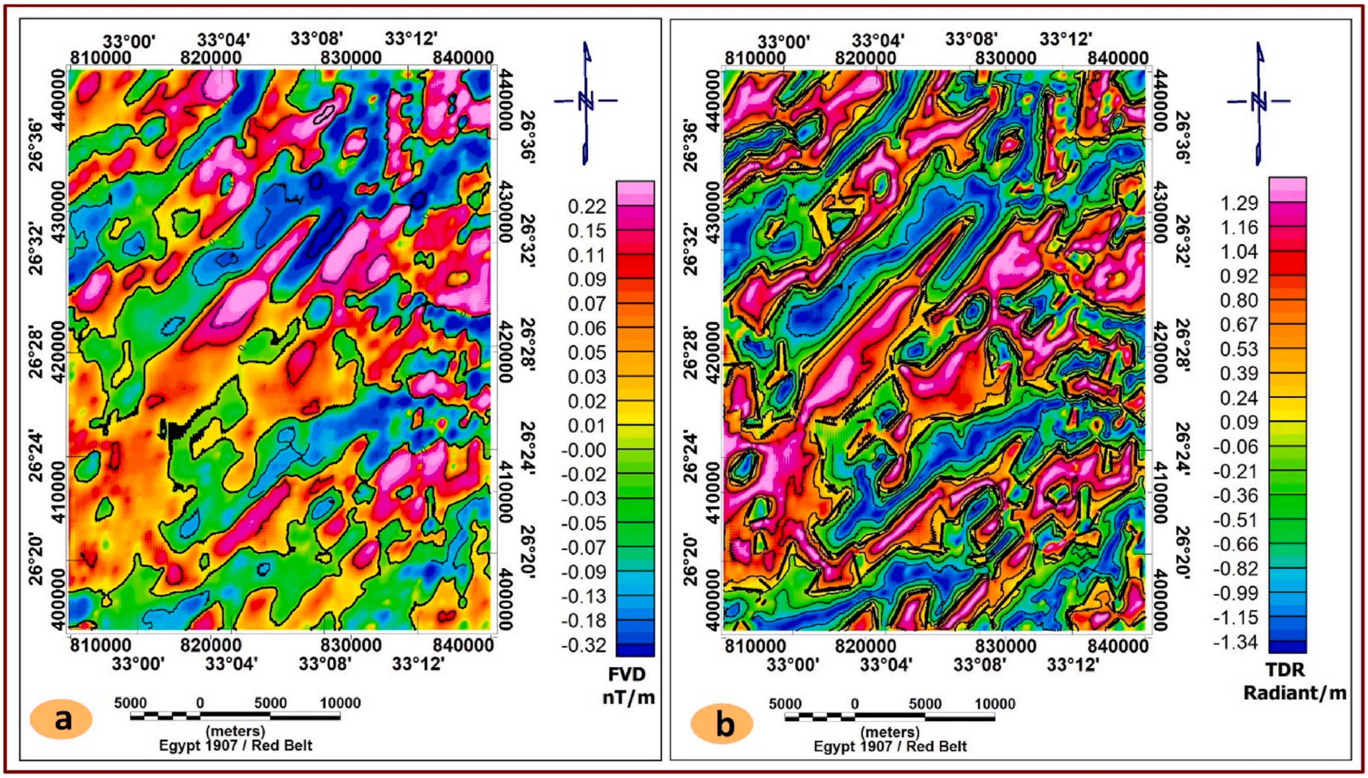

Fig. 10. a) First vertical derivative map; and **b)** Tilt Derivative map of the study area.

reveals prominent geological features and structural boundaries. Distinct magnetic edges are observed mainly in the eastern and western parts of the study area, exhibiting dominant NW-SE and NE-SW orientations. These trends likely correspond to major fault systems and lithological contacts affecting the shallow subsurface, and they are consistent with the regional tectonic framework of the area.

5.3.6. *Tilt derivative (TDR)*

This method is defined as the ratio of the vertical derivative to the total horizontal gradient of the magnetic field and is characterized by values close to zero directly over the edges of causative bodies, making it particularly useful for delineating subsurface contacts and faults. In this study, the tilt derivative was computed from the RTP magnetic data, and the resulting map (Fig. 10b). The zero-contour lines of the tilt derivative were used to trace magnetic susceptibility contrasts, which commonly correspond to lithological boundaries or fault zones. The interpreted structural patterns reveal that the dominant fault orientations within the study area trend NW-SE and NE-SW, consistent with the regional tectonic framework and other magnetic derivative analyses.

5.3.7. *Euler deconvolution method (ED)*

In the present study, structural index values ranging from 0 to 3 were tested. The most reliable solutions were obtained using a structural index of SI = 0, which is typically associated with geological contacts. The resulting Euler solutions for the RTP magnetic anomaly data are shown in (Fig. 11a). These solutions indicate that the depths to subsurface contacts within the study area vary widely, ranging from less than 51.6 m to greater than 692.6 m below the surface, suggesting the presence of both shallow and deep-seated structural features.

5.4. *Structural interpretation*

The interpreted structural map of the study area (Fig. 11b) was constructed by integrating the results derived from the magnetic data analysis, including anomaly patterns, derivative maps, and edge-detection techniques. This map outlines the principal structural framework that has governed the tectonic evolution and geological configuration of the area. The dominant structural lineaments exhibit NE-SW, NW-SE, and N-S orientations (Fig. 11c), reflecting the influence of multiple tectonic regimes and successive deformation phases. These trends are consistent with regional fault systems and suggest a complex structural history involving reactivation of pre-existing weaknesses within the crust. Shear zones represent some of the most significant structural features identified on the interpreted map, particularly with respect to their geological and economic importance. These zones of concentrated deformation, developed under brittle to ductile conditions, enhance the permeability of the host rocks through the development of dense networks of fractures, faults, and vein systems. Such structural pathways facilitate the upward migration of hydrothermal fluids derived from deep crustal or magmatic sources. Variations in physical and chemical conditions within the shear zones, such as changes in pressure, temperature, redox state, or fluid composition, promote the precipitation of dissolved metals, including gold, copper, and sulfide minerals. As a result, shear zones commonly serve both as conduits for mineralizing fluids and as favorable sites for ore deposition, making them prime targets in mineral exploration programs.

Within the study area, three major shear zones, designated S1, S2, and S3, have been delineated along the northeastern and eastern sectors of the interpreted structural map (Fig. 11b). Their spatial association with prominent magnetic lineaments suggests that they are deeply rooted structures, potentially extending to considerable depths. These shear zones may have played a critical role in controlling fluid flow and mineralization processes, highlighting their significance in understanding the tectonic evolution and mineral potential of the area.

6. Conclusion

The integrated radiometric and magnetic survey of the Kulet Niheidat-Abu Had area, Central Eastern Desert of Egypt, provides critical insights into the distribution of naturally occurring radioactive elements and their geological significance. The elevated uranium anomalies, particularly within the Duwi Formation and younger granitic intrusions, highlight zones of potential economic interest and warrant further geochemical and mineralogical investigations. The thorium and potassium distributions reinforce the lithological control on radioelement enrichment, while radiogenic heat production values emphasize the role of crystalline rocks in shaping the regional geothermal regime. Magnetic data interpretation reveals a complex structural framework dominated by Northwest–Southeast and Northeast–Southwest fault systems and shear zones, which act as conduits for hydrothermal fluid migration and mineral deposition. Importantly, radiation exposure and

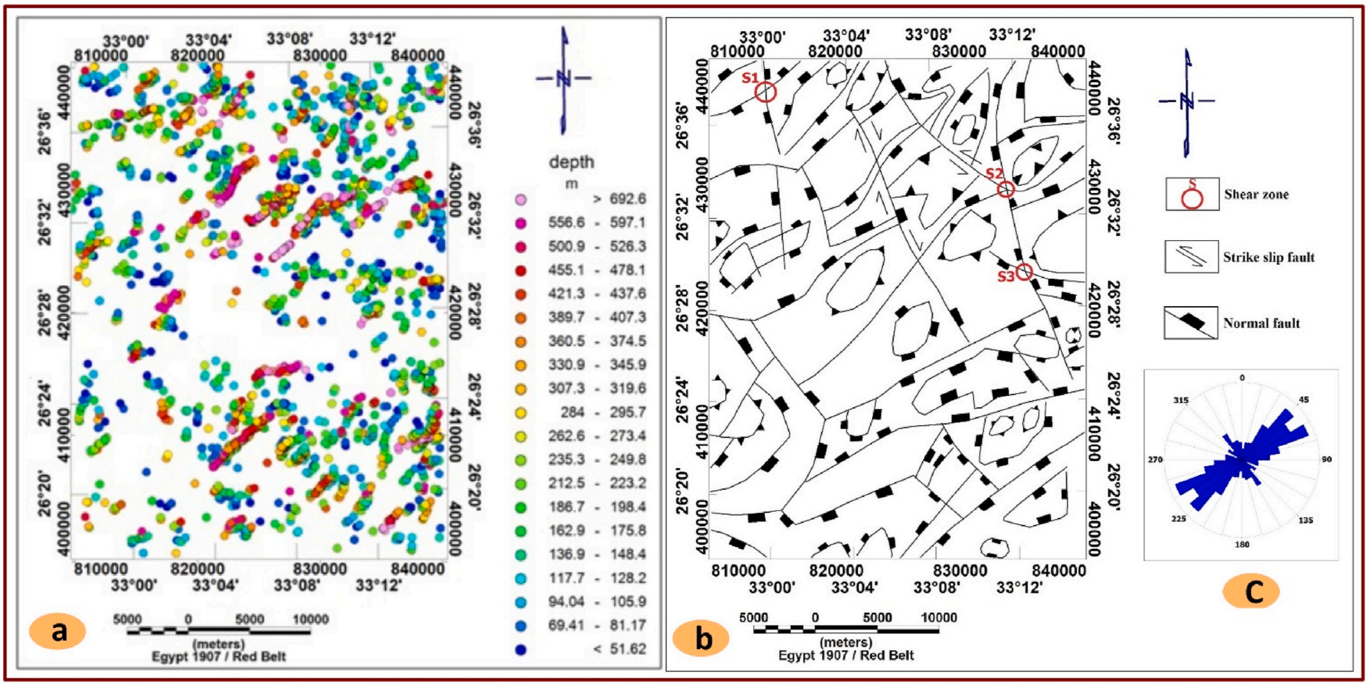

Fig. 11. **a**) Euler deconvolution map of the study area; **b**) Interpreted magnetic structures map; and c) Rose diagram of magnetic structural elements of the study area.

dose rates remain within internationally accepted limits, confirming the absence of immediate environmental or health hazards. This study demonstrates the effectiveness of combining gamma-ray spectrometry with magnetic analysis for delineating uranium anomalies, assessing environmental safety, and understanding the tectonic evolution of the Arabian-Nubian Shield. The results not only advance the geological knowledge of the Central Eastern Desert but also provide a foundation for future exploration programs targeting uranium and associated mineral resources.

CRediT authorship contribution statement

Waheed H. Mohamed: Writing – review & editing, Writing – original draft, Investigation, Formal analysis, Data curation, Conceptualization. **Tamader Alhazani:** Writing – review & editing, Visualization, Resources. **Mohamed Elsadek M. Sabra:** Writing – original draft, Investigation, Conceptualization. **Basma A. El-Badry:** Writing – review & editing, Resources, Funding acquisition. **Mabrouk Sami:** Writing – review & editing, Supervision, Investigation. **Ioan V. Sanislav:** Writing – review & editing, Resources. **El Saeed R. Lasheen:** Writing – review & editing, Investigation, Data curation, Conceptualization.

Availability of data

The analyzed data is included in this paper.

Ethical approval

No investigation on human subjects in this paper.

Funding

This work was supported and funded by the Deanship of Scientific Research at Imam Mohammad Ibn Saud Islamic University (IMSIU) (grant number IMSIU-DDRSP2602).

Conflict of interest

None.

References

Abbady, A. G. E., Uosif, M. A. M., & El-Taher, A. (2005). Natural radioactivity and dose assessment for phosphate rocks from Wadi El-Mashash and El-Mahamid mines, Egypt. *Journal of Environmental Radioactivity, 84*(1), 65–78. https://doi.org/10.1016/j.jenvrad.2005.04.003

Abdel-Aal, M. M., Tawfik, F. S., & Kandil, N. M. (2024). Radiation dose assessments for generic nuclear power plants part I: Routine operation. *Applied Radiation and Isotopes, 211*, Article 111412. https://doi.org/10.1016/j.apradiso.2024.111412

Abdelaal, A., El-Badry, B. A., Saleh, G. M., Sami, M., Khouqeer, G. A., Sanislav, I. V., & Lasheen, E. S. R. (2025). Heavy metal contamination and assessment of radioactivity in coastal sediments: A case study from the El Qulaan area, southern Red Sea, Egypt. *Frontiers in Environmental Science, 13*, Article 1676645. https://doi.org/10.3389/fenvs.2025.1676645

Aero-Service. (1984). *Final operational Report of Airborne Magnetic/Radiation Survey in the Eastern desert, Egypt; for the egyptian general petroleum corporation (EGPC) and the Egyptian geological survey and mining authority (EGSMA)*. TX, USA: Aero-Service: Houston.

Akpanowo, M., Umaru, I., Iyakwari, S., Joshua, E. O., Yusuf, S., & Ekong, G. B. (2020). Determination of natural radioactivity levels and radiological hazards in environmental samples from artisanal mining sites of Anka, North-West Nigeria. *Scientific African, 10*. https://doi.org/10.1016/j.sciaf.2020.e00561

AlZahrani, J. H., Alharbi, W. R., & Abbady, A. G. E. (2011). Radiological impacts of natural radioactivity and heat generation by radioactive decay of phosphorite deposits from northwestern Saudi Arabia. *Australian Journal of Basic and Applied Sciences, 5*(6), 683–690.

Baturin, C. N., & Kochenov, A. V. (2001). Uranium in phosphorites. *Lithology and Mineral Resources, 36*, 303–321.

Blakely, R. J. (1995). *Potential theory in gravity and magnetic applications* (1st ed.). Cambridge University Press. https://doi.org/10.1017/CBO9780511549816

Bücker, C., & Rybach, L. (1996). A simple method to determine heat production from gamma-ray logs. *Marine and Petroleum Geology, 13*(4), 373–375. https://doi.org/10.1016/0264-8172(95)00089-5

Dobrin, M. B., & Savit, C. H. (1961). Introduction to geophysical prospecting. *Bulletin of the Seismological Society of America, 51*(1), 131. https://doi.org/10.1785/BSSA0510010131B, 131.

EGSMA. (1981). *Geological map of Egypt scale1:2,000,000, EGSMA*. Cairo: Ministry of Industry and Mineral Resources.

Eisenbud, M., & Gesell, T. F. (Eds.). (1997). *Environmental radioactivity: From natural, industrial, and military sources* (4th ed.). Academic Press.

El-Qassas, R. A. Y., Abu-Donia, A. M., & Omar, A. E. A. (2023). Delineation of hydrothermal alteration zones associated with mineral deposits, using remote sensing and airborne geophysics data. A case study: El-bakriya area, Central Eastern desert, Egypt. *Acta Geodaetica et Geophysica, 58*(1), 71–107. https://doi.org/10.1007/s40328-023-00405-y

El-Sawy, E. K., Bekhiet, M. H., El-Motaal, E. A., & Orabi, A. A. (2011). Geo-Environmental studies on wadi QENA, Eastern Desert, Egypt. BY using remote sensing data and gis. *Al-Azhar Bulletin of Science, 22*(Issue 2-D), 33–60. https://doi.org/10.21608/absb.2011.7909

Geosoft Program (Oasis Montaj). (2014). *Aero service company, mineral petroleum Groundwater assessment program (MAGMAP), 2-D frequency-domain processing*. Toronto, Canada: Geosoft Inc.

Guo, X., Yan, J., & Wang, Q. (2020). Monitoring of gamma radiation in aseiseic region and its response to seismic events. *Journal of Environmental Radioactivity, 213*, Article 106119. https://doi.org/10.1016/j.jenvrad.2019.106119

Henderson, R. G., & Zietz, I. (1949). THE COMPUTATION OF SECOND VERTICAL DERIVATIVES OF GEOMAGNETIC FIELDS*Presented at the St. Louis meeting of the society, march 16, 1949. Manuscript received by the editor April 12, 1949. Published by permission of the director, U. S. Geological survey. *Geophysics, 14*(4), 508–516. https://doi.org/10.1190/1.1437558

Hervé, A. (2010). Coefficient of variation. *Encyclopedia of Research Design, 1*(5), 169–171.

IAEA. (2010). *Radioelement mapping*. International Atomic Energy Agency.

Lasheen, E. S. R., El-Badry, B. A., Kamh, S. Z., Sami, M., AbdelAll, N., Sanislav, I. V., Hasan, S. S., & Saleh, G. M. (2025). Multispectral remote sensing and radiometric data for delineating radioelement-enriched zones and their health hazards in Um Domi area, South Eastern Desert, Egypt. *Journal of Radiation Research and Applied Sciences, 18*(4), Article 102007. https://doi.org/10.1016/j.jrras.2025.102007

Lasheen, E. S. R., El-Badry, B. A., Mohamed, W. H., Khouqeer, G. A., Sanislav, I. V., & Sami, M. (2025). Radioactivity and aeromagnetic of magmatic suites, Arabian Nubian shield: Petrological and health risk characteristics. *Journal of Radiation Research and Applied Sciences, 18*(4), Article 101910. https://doi.org/10.1016/j.jrras.2025.101910

Lasheen, E. S. R., Elyaseer, M. H., Mohamed, W. H., Azer, M. K., Rashwan, M. A., & Thabet, I. A. (2024). Economic feasibility of Gabal Um Takha leucogranitic intrusion, South Sinai, Egypt: Integrated remote sensing, geochemical, aeromagnetic, and geotechnical approach. *Physics and Chemistry of the Earth, Parts A/B/C, 133*, Article 103531. https://doi.org/10.1016/j.pce.2023.103531

Lasheen, E. S. R., Mohamed, W. H., Elyaseer, M. H., Rashwan, M. A., & Azer, M. K. (2023). Geochemical and remote sensing integrated with satellite gravity data of Darhib and atshan talc deposits, south eastern desert, Egypt. *Scientific Reports, 13*(1), 9108. https://doi.org/10.1038/s41598-023-31398-x

Lasheen, E. S. R., Sami, M., Hegazy, A. A., Arman, H., Sanislav, I. V., Ahmed, M. S., & Rashwan, M. A. (2024). Petrological characteristics and physico-mechanical properties of dokhan volcanics for decorative stones and building material applications. *Buildings, 14*(11), 3418. https://doi.org/10.3390/buildings14113418

Lasheen, E. S. R., Semary, H. E., Kamh, S. Z., & Saleh, G. M. (2026). Advanced remote sensing techniques for mapping lithological units and radioactive alteration in the Southern eastern desert, Egypt: Petrological and radiological hazards determination. *Advances in Space Research*. https://doi.org/10.1016/j.asr.2025.12.109. S0273117725015522.

Lasheen, E. S. R., Zakaly, H. M. H., Alotaibi, B. M., Saadawi, D. A., Ene, A., Fathy, D., Awad, H. A., & El Attar, R. M. (2022). Radiological risk parameters of the phosphorite deposits, gebel qulu El sabaya: Natural radioactivity and geochemical characteristics. *Minerals, 12*(11), 1385. https://doi.org/10.3390/min12111385

Miller, H. G., & Singh, V. (1994). Potential field tilt—A new concept for location of potential field sources. *Journal of Applied Geophysics, 32*(2–3), 213–217. https://doi.org/10.1016/0926-9851(94)90022-1

Mushayandebvu, M. F., Van Driel, P., Reid, A. B., & Fairhead, J. D. (2001). Magnetic source parameters of two-dimensional structures using extended euler deconvolution. *Geophysics, 66*(3), 814–823. https://doi.org/10.1190/1.1444971

Nairy, K., & Aruna Rao, K. (2003). Tests of coefficients of variation of normal population. *Communications in Statistics - Simulation and Computation, 32*(3), 641–661. https://doi.org/10.1081/SAC-120017854

Saada, S. A. (2016). Edge detection and depth estimation of galala El bahariya Plateau, Eastern desert-egypt, from aeromagnetic data. *Geomechanics and Geophysics for Geo-Energy and Geo-Resources, 2*(1), 25–41. https://doi.org/10.1007/s40948-015-0019-6

Saleh, G. M., Kamar, M. S., Khaleal, F. M., Azer, M. K., Nasr, T., & Lasheen, E. S. R. (2025). Petrogenesis and tectonic evolution of tourmaline- bearing leucogranites, Sikait area, Southeastn desert of Egypt utilizing mineralogical and bulk rock analysis. *Scientific Reports, 15*(1), Article 20191. https://doi.org/10.1038/s41598-025-06155-x

Sharma, P. K., Johri, N. K., Raut, G. B., Rangaswamy, G., Pandey, B. K., & Chaturvedi, A. K. (2018). Construction and characterization of transportable calibration pads for calibration of portable and airborne gamma ray spectrometers in India. *Journal of the Geological Society of India, 92*(3), 281–285. https://doi.org/10.1007/s12594-018-1005-8

Spector, A. (1975). *Pplication of aeromagnetic data for porphyry copper exploration in areas of volcanic cover, the 45th Ann. Inter. Meeting of the Society of exploration geophysics*. October 15, Denver, Colorado, U.S.

Thompson, D. T. (1982). EULDPH: A new technique for making computer-assisted depth estimates from magnetic data. *Geophysics, 47*(1), 31–37. https://doi.org/10.1190/1.1441278

Verduzco, B., Fairhead, J. D., Green, C. M., & MacKenzie, C. (2004). New insights into magnetic derivatives for structural mapping. *The Leading Edge, 23*(2), 116–119. https://doi.org/10.1190/1.1651454

Youssef, M. A. S., & Elkhodary, S. T. (2013). Utilization of airborne gamma ray spectrometric data for geological mapping, radioactive mineral exploration and environmental monitoring of southeastern Aswan city, South Eastern desert, Egypt. *Geophysical Journal International, 195*(3), 1689–1700. https://doi.org/10.1093/gji/ggt375